

Integrability Breaking and Coherent Dynamics in Hermitian and Non-Hermitian Spin Chains with Long-Range Coupling

Y. S. Liu and X. Z. Zhang*

College of Physics and Materials Science, Tianjin Normal University, Tianjin 300387, China

Unraveling the mechanisms of ergodicity breaking in complex quantum systems is a central pursuit in nonequilibrium physics. In this work, we investigate a one-dimensional spin model featuring a tunable long-range hopping term, H_n , which introduces nonlocal interactions and bridges the gap between Hermitian and non-Hermitian regimes. Through a systematic analysis of level-spacing statistics, Krylov complexity, and entanglement entropy, we demonstrate that H_n acts as a universal control parameter driving the transition from integrability to quantum chaos. Specifically, increasing the strength of H_n induces a crossover from Poissonian to Gaussian Orthogonal Ensemble statistics in the Hermitian limit, and similarly triggers chaotic dynamics in the non-Hermitian case. Most remarkably, despite the onset of global chaos, we identify a tower of exact nonthermal eigenstates that evade thermalization. These states survive as robust quantum many-body scars, retaining low entanglement and coherent dynamics even under strong non-Hermitian perturbations. Our findings reveal a universal mechanism by which long-range and non-Hermitian effects reshape quantum ergodicity, offering new pathways for preserving quantum coherence in complex many-body systems.

I. INTRODUCTION

A central pursuit in modern quantum physics is to understand how quantum coherence can persist in complex, interacting many-body systems—an essential requirement for scalable quantum technologies and fundamental to nonequilibrium statistical mechanics [1–6]. In generic isolated systems, coherence is rapidly lost as the system thermalizes, a process captured by the Eigenstate Thermalization Hypothesis (ETH) [7–15]. According to the ETH, each eigenstate behaves thermally with respect to local observables, implying that any initial state evolves toward a Gibbs ensemble and forgets its microscopic details. Yet, numerous mechanisms are now known to evade this fate. Integrable systems maintain an extensive set of conserved quantities that constrain their dynamics, while many-body localization (MBL) suppresses transport and thermalization through disorder-induced emergent integrals of motion [16–21]. More recently, the discovery of quantum many-body scars (QMBS) has revealed a subtler route to ergodicity breaking [22–27]. In these systems, a small subspace of atypical, low-entanglement eigenstates coexists within an otherwise thermal spectrum. When the system is initialized with finite overlap on this subspace, it exhibits long-lived oscillations and nonthermal dynamics despite the surrounding chaotic background.

However, truly isolated systems are an abstraction. In realistic settings, interaction with the environment—through dissipation, loss, or measurement—inevitably renders the dynamics non-Hermitian (NH) [28–31]. Non-Hermitian Hamiltonians thus provide a powerful framework to model open quantum systems, capturing both gain–loss processes and conditional evolution [29, 32, 33]. This extension challenges conventional notions of thermalization and chaos: when the spectrum becomes complex, the familiar diagnostics of integrability based on real-level statistics cease to apply.

To address this, new spectral measures have been introduced, including the complex spacing ratio (CSR) [34–36] and singular-value statistics [35, 37], which generalize random matrix theory (RMT) concepts to the complex plane. Yet, despite these advances, the interplay between non-Hermiticity, integrability breaking, and ergodicity remains only partially understood. In particular, the fate of quantum many-body scars in systems that are simultaneously non-Hermitian and nonintegrable remains an open and largely unexplored problem.

In this work, we address this challenge by studying a one-dimensional spin-1 model that includes a tunable long-range hopping term H_n . This term, controlled by a complex coupling J_n , introduces nonlocal interactions and provides a unified knob for driving the system from the Hermitian to the non-Hermitian regime. We demonstrate that H_n acts as a universal integrability-breaking mechanism: in the Hermitian case, increasing J_n induces a clear transition from Poissonian to Gaussian Orthogonal Ensemble (GOE) statistics, whereas in the non-Hermitian case, a complex J_n produces an analogous crossover characterized by CSR and Krylov complexity. Our key finding is that a tower of exact, nonthermal eigenstates, originating from the integrable limit, survives both Hermitian and non-Hermitian perturbations. These states retain low entanglement and give rise to coherent fidelity revivals even deep in the chaotic regime. This persistence reveals a striking robustness of scarred subspaces against both nonlocal interactions and non-Hermitian deformations, suggesting a universal mechanism by which quantum coherence can persist beyond conventional integrable settings.

The remainder of this paper is organized as follows. Section II introduces the model Hamiltonian and its symmetry structure, and derives the exact ferromagnetic tower of eigenstates. Section III analyzes the Hermitian regime, mapping the integrability-to-chaos transition using level statistics and Krylov complexity, and identifies the persistence of scars through entanglement and fidelity diagnostics. Section IV extends this analysis to the non-Hermitian regime, employing CSR and dynamical measures to confirm a parallel transition

* zhangxz@tjnu.edu.cn

and the survival of the scar states. Section V concludes with a summary and outlook. Technical derivations and computational methods are provided in Appendices A and B.

II. MODEL HAMILTONIAN

Tremendous efforts have been devoted to exploring the transition from integrable to non-integrable dynamics in quantum many-body systems, particularly in spin-1/2 chains, where the breaking of integrability is typically induced by disorder or kinetic constraints [15, 38–44]. In contrast, here we demonstrate that a spin-1 chain with long-range spin-orbital coupling can host a tower of many-body scar states residing in arbitrary energy sectors modulated by an external magnetic field. The model Hamiltonian is given by

$$H = J_h H_h + J_c H_c + J_z H_z + \sum_n J_n H_n, \quad (1)$$

where H_h , H_c , H_z , and H_n denote Hermitian operators describing distinct physical interactions. The coefficients J_h , J_c , J_z , and J_n characterize the relative strength and phase of the corresponding processes. Their complex nature implies that the Hermiticity of the full Hamiltonian is not guaranteed and depends sensitively on microscopic control parameters.

The first term

$$H_h = \sum_{j=1}^N \mathbf{S}_j \cdot \mathbf{S}_{j+1} \quad (2)$$

represents the spin-1 Heisenberg exchange interaction. At each lattice site j the spin operators $\mathbf{S}_j = (S_j^x, S_j^y, S_j^z)$ satisfy the usual SU(2) commutation relations

$$[S_j^\alpha, S_k^\beta] = i\delta_{jk} \sum_\gamma \varepsilon_{\alpha\beta\gamma} S_j^\gamma, \quad \alpha, \beta, \gamma \in \{x, y, z\}, \quad (3)$$

where $\varepsilon_{\alpha\beta\gamma}$ is the Levi-Civita symbol, defined as

$$\varepsilon_{\alpha\beta\gamma} = \begin{cases} +1, & \text{if } (\alpha\beta\gamma) = (xyz), (yzx), (zxy), \\ -1, & \text{if } (\alpha\beta\gamma) = (xzy), (yxz), (zyx), \\ 0, & \text{if any two indices are equal,} \end{cases} \quad (4)$$

. The ladder operators are defined in the standard manner:

$$S_j^\pm \equiv S_j^x \pm iS_j^y, \quad (5)$$

$$[S_j^z, S_k^\pm] = \pm\delta_{jk} S_j^\pm, \quad (6)$$

$$[S_j^+, S_k^-] = 2\delta_{jk} S_j^z. \quad (7)$$

In the S^z -basis the single-site eigenstates are labeled by $m_j \in \{+1, 0, -1\}$ so that $S_j^z|m_j\rangle = m_j|m_j\rangle$ and $S_j^+|+1\rangle = 0$, $S_j^-|-1\rangle = 0$. The global (total) spin operators are

$$S^\pm \equiv \sum_{j=1}^N S_j^\pm, \quad S^z = \sum_{j=1}^N S_j^z. \quad (8)$$

Experimentally, this term can be realized in ultracold atomic gases confined in optical lattices, where effective spin-1 degrees of freedom arise from hyperfine manifolds of alkali atoms such as ^{23}Na or ^{87}Rb [45–47]. The superexchange interaction between neighboring lattice sites gives rise to the effective coupling J_h , whose magnitude and sign can be tuned via optical lattice depth and spin-dependent collisions [48–50].

The second term describes a chiral three-spin interaction,

$$H_c = \sum_{j=1}^N \mathbf{S}_j \cdot (\mathbf{S}_{j+1} \times \mathbf{S}_{j+2}), \quad (9)$$

which breaks both time-reversal and inversion symmetries [51]. Such a chiral coupling can emerge in spin-orbit-coupled Mott insulators through higher-order superexchange processes or be engineered synthetically in Rydberg-atom arrays and trapped-ion platforms via Floquet modulation schemes that imprint complex tunneling phases [52–55]. The strength J_c can thus be dynamically tuned by adjusting the driving amplitude or the relative phase between neighboring bonds.

The third term

$$H_z = \sum_{j=1}^N S_j^z \quad (10)$$

is the Zeeman coupling between the local spin and an external magnetic field along the z direction. This term can be directly controlled by the applied magnetic field strength or by effective AC-Stark shifts in optical or microwave dressing schemes, enabling selective tuning of the on-site energy splitting [56].

Finally, the nonlocal hopping term

$$H_n = i \sum_{j=1}^N (S_j^+ S_{j+n}^- - S_j^- S_{j+n}^+), \quad (11)$$

represents a long-range spin-exchange process with hopping distance n , where

$$n = \begin{cases} 1, 2, \dots, N/2 - 1, & N \text{ even,} \\ 1, 2, \dots, (N-1)/2, & N \text{ odd,} \end{cases} \quad (12)$$

under periodic boundary conditions (PBC). The term H_n naturally arises in systems with long-range dipole–dipole or spin-orbit-mediated interactions, such as polar molecules, trapped ions, or cavity-QED arrays. In such platforms, the coupling strength J_n can be rendered complex by controlling laser-induced Raman transitions, thereby introducing tunable synthetic gauge phases. In particular, trapped-ion quantum simulators have demonstrated laser-mediated spin couplings whose interaction range scales inversely with system size, successfully engineering long-range effective interactions [57].

A. Symmetries, and Exact Ferromagnetic States

1. Symmetries

We now summarize the symmetry structure of H . (i) U(1) symmetry: Each term in H commutes with the total magnetization $S^z = \sum_j S_j^z$, i.e., $[S^z, H_k] = 0$ for $k = h, c, z, n$.

Thus S^z (or equivalently the total magnetization $M \equiv S^z$) is a constant of motion and the full Hilbert space decomposes into orthogonal magnetization sectors

$$H = \bigoplus_{M=-N}^{+N} \mathcal{H}_M, \quad (13)$$

where

$$\mathcal{H}_M \equiv \{ |\psi(p)\rangle : S^z |\psi(p)\rangle = M |\psi(p)\rangle \}. \quad (14)$$

We will often parametrize a sector by the number of spin-lowering operations p relative to the fully polarized state (see below), so that $M = N - p$, where $p = 0, 1, 2, \dots, 2N$. (ii) Lattice translation symmetry: Assuming uniform couplings and PBC, the Hamiltonian is invariant under the one-site translation operator T . Hence, crystal momentum k is a good quantum number, and each sector \mathcal{H}_M further splits into $\mathcal{H}_M = \bigoplus_k \mathcal{H}_{M,k}$, where $T |\psi_{M,k}\rangle = e^{ik} |\psi_{M,k}\rangle$. (iii) Global SU(2) symmetry: The Heisenberg term H_h and the chiral term H_c are rotational scalars, satisfying $[S^2, H_{h/c}] = 0$ and $[S^\alpha, H_{h/c}] = 0$ ($\alpha = x, y$) [15, 51]. However, the subgroup generated by S^z and term H_z and the nonlocal term H_n break the full SU(2) symmetry down to the $U(1)$. Consequently, the total spin \mathbf{S}^2 is not a conserved quantity for the generic Hamiltonian.

2. Symmetry-determined subspaces

Collecting the results above, the Hamiltonian block-diagonalizes into symmetry-labeled subspaces. A convenient labeling is

$$H = \bigoplus_{M=-N}^N \bigoplus_k \mathcal{H}_{M,k}, \quad (15)$$

where M (total S^z) and k (crystal momentum) are exact quantum numbers for the full Hamiltonian defined above. If additionally $J_z = J_n = 0$ (pure SU(2)-symmetric point), each (M, k) block further decomposes into irreducible SU(2) multiplets labeled by total spin S_{tot} (eigenvalues of \mathbf{S}^2). If $J_c = 0$ and all coefficients are real, spatial parity may also be a symmetry and can be used to refine the block decomposition; the presence of H_c usually removes parity as a good quantum number.

3. Exact ferromagnetic tower of states

Despite the complex structure of H , it possesses an exactly solvable tower of ferromagnetic states. These states are the totally symmetric (zero-momentum) multiplet generated from the fully polarized highest-weight state $|\uparrow\rangle \equiv \bigotimes_{j=1}^N |+1\rangle_j$:

$$|\psi(N, N - p)\rangle \equiv \frac{1}{\Omega} (S^-)^p |\uparrow\rangle \quad (16)$$

where $\Omega = \sqrt{(2N)!p!/(2N - p)!}$. We can find their eigenenergies by evaluating the action of each term on this tower. First, the highest-weight state $|\uparrow\rangle$ is a trivial eigenstate of all four terms: $H_h |\uparrow\rangle = N |\uparrow\rangle$ (since each neighboring pair of fully aligned spin-1 moments satisfies $S_j \cdot S_{j+1} |\uparrow\rangle = 1$, corresponding to a normalized contribution of +1 per bond), $H_c |\uparrow\rangle = 0$ (as the scalar triple product of parallel vectors vanishes), $H_z |\uparrow\rangle = N |\uparrow\rangle$, and $H_n |\uparrow\rangle = 0$ (due to $S_j^+ |+1\rangle_j = 0$).

Because H_h and H_c are rotational scalars, they commute with S^- and thus act invariantly on the entire tower, yielding $H_h |\psi(N, N - p)\rangle = N |\psi(N, N - p)\rangle$ and $H_c |\psi(N, N - p)\rangle = 0$ for all p . The Zeeman term acts as $H_z |\psi(N, N - p)\rangle = (N - p) |\psi(N, N - p)\rangle$, which follows from $[S^z, (S^-)^p] = -p (S^-)^p$. Finally, the nonlocal term H_n annihilates every state in the tower, $H_n |\psi(N, N - p)\rangle = 0$. This arises because $|\psi(N, N - p)\rangle$ is the $k = 0$ (totally symmetric) p -magnon state, and the antisymmetric structure of the H_n operator [Eq. (11)] results in a vanishing eigenvalue for this uniform superposition (see Appendix A for more details).

Combining these results, we find that the states $|\psi(N, N - p)\rangle$ are exact eigenstates of the full Hamiltonian [Eq. (1)] with energies

$$H |\psi(N, N - p)\rangle = E(p) |\psi(N, N - p)\rangle, \quad (17)$$

$$E(p) = J_h N + J_z (N - p). \quad (18)$$

This tower of exact states spans all magnetization sectors $M = N - p$, featuring an energy spectrum that varies linearly with M . Remarkably, these states remain robust even in the presence of the non-integrable interactions H_c and H_n .

Here two points should be highlighted: 1. The crucial property that makes the states Eq. (16) exactly solvable is that they are the totally symmetric (zero-momentum) multiplet generated from the highest-weight state $|\uparrow\rangle$. Any Hamiltonian that (i) acts as a scalar on this multiplet (e.g. SU(2)-invariant two- and three-spin scalar operators) and (ii) annihilates the uniform magnon superposition (as H_n does in the antisymmetric form above) will preserve the tower. 2. If one perturbs the model by terms that break translation invariance (disorder) or introduce momentum-dependent hopping that does not annihilate the $k = 0$ magnon, the tower generically hybridizes with other states and ceases to be exact; nevertheless, for sufficiently weak perturbations the tower may survive as long-lived scarred eigenstates (quasi-exact).

In the following sections, we will explore the spectral and dynamical properties of this model and demonstrate how a tower of nonthermal eigenstates persists despite the presence of non-integrable, long-range interactions. For simplicity, in the subsequent analysis, we focus on the case with a single $n = 3$ term. Nevertheless, calculations performed with the full Hamiltonian in Eq. (1), which includes the summation over all H_n , yield qualitatively similar results.

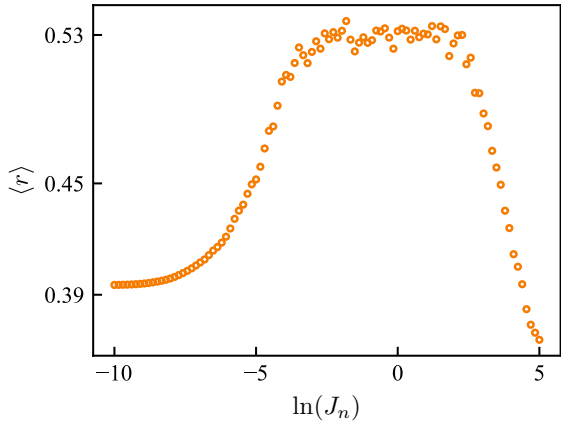


FIG. 1. Dependence of the average level spacing ratio $\langle r \rangle$ on the non-local hopping strength J_n . Calculations are performed for a system with parameters $(J_h, J_c, J_z, n) = (1, 1, 0.5, 3)$ under PBC. As J_n increases, the system exhibits a clear transition from an integrable regime to a chaotic one, and eventually reenters the integrable regime at large J_n . Results correspond to a system size of $N = 12$, within the $(M, k) = (0, 0)$ subspace whose Hilbert-space dimension is 6166.

III. SPECTRAL STATISTICS AND QUANTUM SCAR IN THE HERMITIAN LIMIT

A. Crossover between the integrability and chaos

Before investigating the emergence of quantum many-body scars and the associated revival dynamics, it is essential to first characterize the integrability of the system in its Hermitian limit. We focus on the case where all coupling constants J_h , J_c , and J_n are real. In this regime, the Hamiltonian remains Hermitian, allowing us to quantify integrability through spectral statistics.

To this end, we analyze the nearest-neighbor level spacings of the Hamiltonian eigenenergies. Denoting the ordered spectrum as $\{E_i\}$, we define the level spacing as $s_i = E_{i+1} - E_i$. The statistical distribution of $\{s_i\}$ serves as a powerful diagnostic for quantum integrability. A particularly robust and widely used indicator is the ratio of adjacent level spacings,

$$r_i = \min\left(\frac{s_{i-1}}{s_i}, \frac{s_i}{s_{i-1}}\right), \quad (19)$$

whose ensemble average $\langle r \rangle$ characterizes the underlying spectral correlations [58]. In integrable systems, energy levels are uncorrelated and follow a Poisson distribution, yielding $\langle r \rangle_{\text{Poisson}} \approx 0.386$. By contrast, non-integrable (chaotic) systems display level repulsion consistent with Wigner-Dyson statistics, where $\langle r \rangle_{\text{GOE}} \approx 0.536$ or $\langle r \rangle_{\text{GUE}} \approx 0.603$, depending on the symmetry class of the system [51, 58].

To identify the role of the nonlocal term H_n , we compare two cases:

$$H_0 = J_h H_h + J_c H_c + J_z H_z, \quad (20)$$

$$H = H_0 + J_n H_n. \quad (21)$$

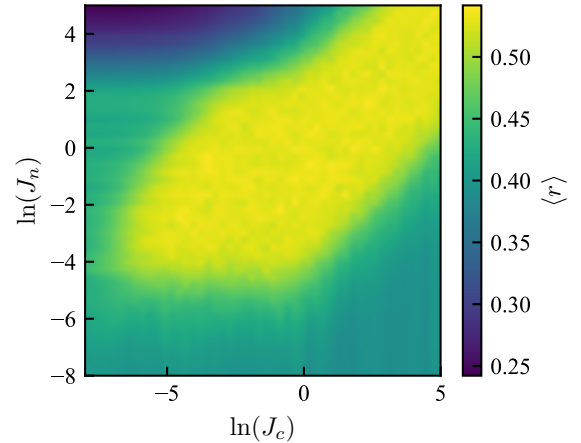


FIG. 2. Phase diagram in the plane of chiral coupling J_c and nonlocal coupling J_n . The color map shows the mean level-spacing ratio $\langle r \rangle$ computed within the $\mathcal{H}_{M=0, k=0}$ symmetry sector for $(J_h, J_z, n) = (1, 0.5, 3)$. The system remains integrable when either J_c or J_n is weak, whereas clear signatures of quantum chaos appear only when both couplings become comparable in magnitude. Data shown are for a system size $N = 12$, corresponding to a Hilbert-space dimension of 6166.

The comparison between H_0 and H allows us to isolate the effect of H_n on integrability. We compute the mean spacing ratio $\langle r \rangle$ as a function of J_n , within the symmetry-resolved subspace $\mathcal{H}_{M=0, k=0}$. As shown in Fig. 1, the system undergoes a crossover from integrability to quantum chaos and then back to near-integrability as J_n increases from zero. This non-monotonic behavior highlights the delicate balance between local and nonlocal spin interactions in shaping the dynamical complexity of the system.

To provide a comprehensive understanding of the model, we systematically analyze two key aspects: the phase diagram of the chiral coupling J_c and the nonlocal coupling J_n in terms of the average level spacing ratio $\langle r \rangle$. The results, presented in Fig. 2, demonstrate that within the studied subspace $(M, k) = (0, 0)$, the system remains in the integrable regime when both coupling parameters J_c and J_n are weak. As J_c and J_n increase, the system gradually transitions from an integrable to a non-integrable regime. Notably, when both couplings become sufficiently strong, the contribution of H_h becomes negligible, yet the system still exhibits non-integrable (chaotic) behavior. This finding highlights that the interplay between H_c and H_n plays a dominant role in determining the transition between integrability and chaos in this model. For $J_n = 0$, the Hamiltonian H_0 corresponds to an integrable model, as evidenced by the Poissonian level-spacing statistics. Introducing a finite, yet small, J_n breaks integrability and drives the system toward the Wigner-Dyson regime, as illustrated by the numerical results shown in panels (a) and (c) of Fig. 3.

This transition serves as the foundation for understanding how weak nonlocal perturbations generate scar-like coherent dynamics in an otherwise chaotic spectrum.

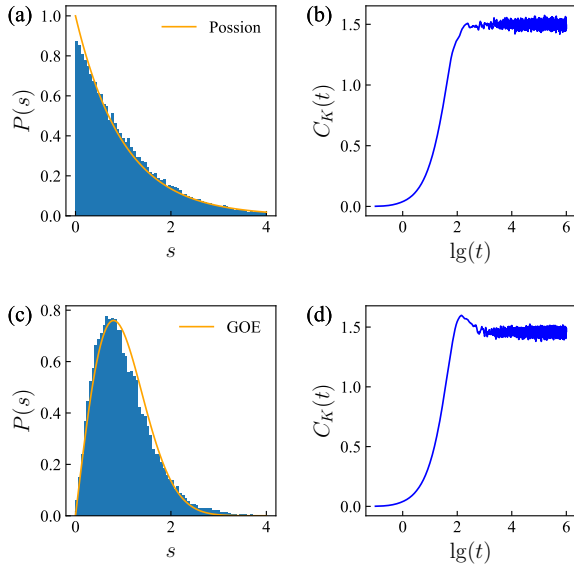


FIG. 3. Distribution of nearest-neighbor level spacings and the corresponding average ratio $\langle r \rangle$ for the central part of the spectrum, together with the time evolution of the Krylov complexity of $\mathcal{H}_{M=0, k=0}$ under periodic boundary conditions. Calculations are performed with parameters $(J_h, J_c, J_z, n) = (1, 1, 0.5, 3)$. For $J_n = 0$, panel (a) shows a Poissonian level-spacing distribution with $\langle r \rangle \approx 0.392$, indicative of integrability, and panel (b) displays the Krylov complexity, which rapidly rises and saturates—characteristic of integrable dynamics. For $J_n = 0.2$, panel (c) exhibits a Gaussian-orthogonal-ensemble (GOE) distribution with $\langle r \rangle \approx 0.529$, signaling the onset of quantum chaos, while panel (d) shows a non-monotonic evolution of the Krylov complexity—initial growth, decay, and eventual saturation—typical of chaotic systems. These results together demonstrate a clear transition from integrability to chaos as J_n increases, consistent with the mean level-spacing ratio defined in Eq. (19). Panels (a) and (c) correspond to a system size of $N = 14$ (Hilbert-space dimension 44046), while panels (b) and (d) correspond to $N = 10$ (dimension 902).

Beyond static spectral diagnostics, the integrable-to-chaotic transition can be further characterized from a dynamical perspective. We employ the Krylov complexity framework, which quantifies how an initial quantum state spreads under repeated action of the Hamiltonian. Operationally, the Krylov basis is constructed through iterative applications of H followed by orthogonalization with respect to the previously generated basis vectors [59–63]. To ensure consistency between the Hermitian and non-Hermitian analyses, we adopt the bi-Lanczos algorithm for numerical implementation. Details of this algorithm are provided in Appendix B. This approach enables us to capture both spectral and dynamical signatures of integrability breaking and to connect them directly to the emergence of many-body scars and revival dynamics.

The bi-Lanczos algorithm maps the time evolution of a quantum state under a (possibly non-Hermitian) Hamiltonian onto an effective single-particle tight-binding model defined on a semi-infinite chain [59]. This mapping provides an intuitive and powerful framework for analyzing the complex dynamical behavior of quantum systems and serves as an efficient

diagnostic tool to distinguish between integrable and chaotic regimes.

To construct the Krylov basis for a non-Hermitian Hamiltonian H , one introduces two sets of biorthogonal basis vectors $\{|q_n\rangle\}$ and $\{|p_n\rangle\}$ satisfying

$$\langle p_m | q_n \rangle = \delta_{mn}, \sum_n |q_n\rangle \langle p_n| = 1, \quad (22)$$

$$|q_0\rangle = |p_0\rangle = |\psi(0)\rangle. \quad (23)$$

The subsequent Krylov vectors are generated recursively through the bi-Lanczos iteration:

$$H|q_n\rangle = a_n|q_n\rangle + b_{n+1}|q_{n+1}\rangle + c_n|q_{n-1}\rangle, \quad (24)$$

$$H^\dagger|p_n\rangle = a_n^*|p_n\rangle + c_{n+1}^*|p_{n+1}\rangle + b_n^*|p_{n-1}\rangle, \quad (25)$$

where the coefficients a_n , b_n , and c_n are determined so that the biorthogonality condition is maintained at each step.

In this Krylov representation, the time-dependent wave function can be expanded as

$$|\psi(t)\rangle = \sum_n \phi_n(t)|q_n\rangle, \quad (26)$$

where $\phi_n(t) = \langle p_n | \psi(t) \rangle$ denotes the projection of the evolving state onto the n -th Krylov vector. The amplitudes $\phi_n(t)$ satisfy a discrete Schrödinger-like equation that resembles a single-particle tight-binding model on a semi-infinite chain:

$$i \frac{\partial}{\partial t} \phi_n(t) = b_n \phi_{n-1}(t) + a_n \phi_n(t) + c_{n+1} \phi_{n+1}(t). \quad (27)$$

Here $\{a_n, b_n, c_n\}$ are the Lanczos coefficients obtained from the bi-Lanczos recursion described in Appendix B 1. This recurrence relation is mathematically equivalent to a tight-binding chain where a_n represents on-site energies and b_n, c_n denote the hopping amplitudes between neighboring sites.

Once the coefficients $\phi_n(t)$ are obtained, the Krylov complexity is defined as [59–63]

$$C_K(t) = \sum_n n |\phi_n(t)|^2, \quad (28)$$

which quantifies the spread of the quantum state in the Krylov space, i.e., how far the evolved state has propagated along the effective chain.

For Hermitian and non-Hermitian systems, the behavior of $C_K(t)$ provides a clear dynamical signature of integrability. In integrable systems, $C_K(t)$ rapidly saturates to a steady plateau, reflecting quasi-periodic and restricted motion in Krylov space. In contrast, for chaotic systems, $C_K(t)$ exhibits a rapid initial growth followed by saturation at a much higher value, signaling extensive spreading across the Krylov basis [60].

Next, within the subspace $(M, k) = (0, 0)$, we compute the Krylov complexity for various values of J_n , using as the initial state the equal-weight linear superposition of the eigenstates of the Hermitian matrix obtained by taking the lower-triangular part of the Hamiltonian and restricting it to this subspace. As shown in panels (b) and (d) of Fig. 3, for $J_n = 0$, the Krylov complexity quickly reaches a steady plateau, consistent with

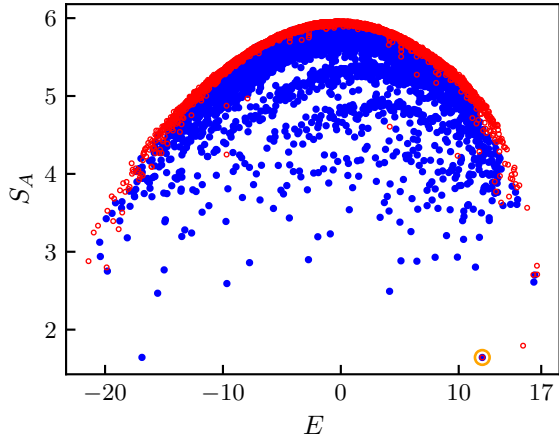


FIG. 4. Von Neumann entanglement entropy, computed using Eq. (30), for a system of size $N = 12$ under periodic boundary conditions (PBC) with parameters $(J_h, J_c, J_z, n) = (1, 1, 0.5, 3)$. Within the $(M, k) = (0, 0)$ subspace (Hilbert-space dimension is 6166), the entanglement entropies of all eigenstates are plotted for $J_n = 0$ (blue dots) and $J_n = 0.2$ (red circles). A notable feature is the persistence of a low-entanglement state in the lower-right region (an orange circle) across the integrable-to-chaotic transition, indicating its robustness as a quantum scar state.

integrable dynamics. Conversely, for $J_n = 0.2$, $C_K(t)$ displays a pronounced growth before saturation, indicative of chaotic evolution. These contrasting behaviors demonstrate that Krylov complexity serves as a sensitive probe distinguishing integrable and chaotic regimes within the same microscopic model.

B. The evidence of the Quantum many-body scars

While the introduction of the nonlocal hopping term H_n drives the system from integrability to chaos, a set of nonthermal states originating from the tower states $\{|\psi_n(N, N-p)\rangle\}$ can persist deep in the chaotic regime. To understand this phenomenon, it is instructive to first discuss the underlying structure of the Hilbert space.

In our spin-1 model, the conservation of the total magnetization $S_{\text{tot}}^z = \sum_j S_j^z$ divides the full Hilbert space into dynamically disconnected subspaces labeled by the quantum number $M = S_{\text{tot}}^z$. This fragmentation implies that the Hamiltonian is block-diagonal, $H = \bigoplus_M \mathcal{H}_M$, and each block \mathcal{H}_M evolves independently under unitary dynamics. Within each fixed- M sector, the tower state Eq. (16) resides as a highly symmetric state with minimal entanglement. These states remain exact eigenstates of the Hamiltonian even when $J_n \neq 0$, demonstrating their robustness against the non-integrable perturbations introduced by H_n . Despite the presence of chaotic dynamics in the remaining spectrum, these exact nonthermal states coexist with thermal eigenstates, a characteristic feature reminiscent of quantum many-body scars.

To characterize the nonthermal nature of these states, we

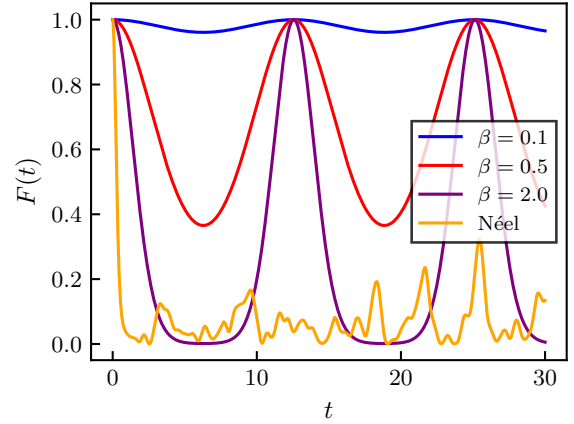


FIG. 5. Fidelity dynamics of the Hamiltonian H with parameters $(J_h, J_c, J_z, J_n, n) = (1, 1, 0.5, 0.2, 3)$ under periodic boundary conditions, for a system size of $N = 8$ with a Hilbert-space dimension of 6561. When the initial state is chosen as the coherent state defined in Eq. (31), clear periodic revivals are observed, indicating that this coherent state, or equivalently, the tower of states defined in Eq. (16), exhibits the characteristic behavior of a quantum many-body scar. In contrast, when initialized in the Néel state, the fidelity rapidly decays to zero, signaling fast thermalization and the absence of scar dynamics.

compute the bipartite entanglement entropy of each eigenstate $|\psi_n\rangle$. The system is divided into two subsystems A and B , and for each eigenstate, we construct the reduced density matrix of subsystem A as

$$\rho_{A,n} = \text{Tr}_B(|\psi_n\rangle\langle\psi_n|), \quad (29)$$

and define the von Neumann entanglement entropy

$$S_A = -\text{Tr}[\rho_{A,n} \ln \rho_{A,n}]. \quad (30)$$

As shown in Fig. 4, the entropy distribution in the chaotic regime displays a sharp dip corresponding to one particular eigenstate whose entanglement remains anomalously low. This state can be directly associated with one member of the tower $\{|\psi_n(N, N-p)\rangle\}$, demonstrating that the tower survives as a scarred subspace even after the system becomes globally nonintegrable.

To further probe the dynamical manifestation of these scarred states, we construct a coherent superposition of the tower states as

$$|\beta\rangle = e^{\beta S^-} |\uparrow\rangle = \sum_{p=0}^{2N} \frac{\beta^p}{p!} |\psi_n(N, N-p)\rangle, \quad (31)$$

and study its fidelity dynamics under time evolution,

$$F(t) = |\langle\beta|e^{-iHt}|\beta\rangle|^2. \quad (32)$$

As shown in Fig. 5, $F(t)$ exhibits pronounced periodic revivals for several choices of β , signaling coherent oscillations characteristic of quantum many-body scars. In contrast, a typical

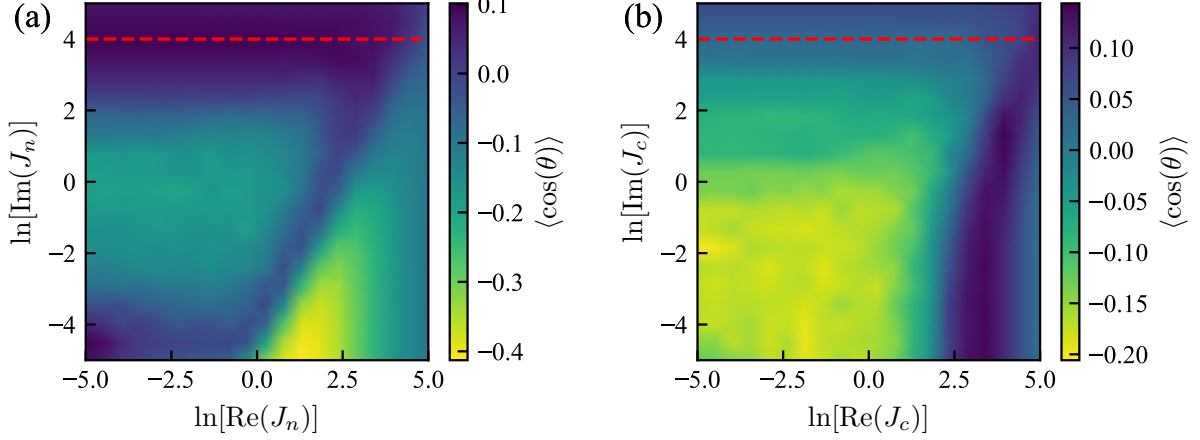


FIG. 6. Phase diagrams of the non-Hermitian spin system under complex coupling parameters (a) J_n and (b) J_c . (a) With J_c fixed at 1, the system exhibits an integrable–nonintegrable–integrable crossover as either the real or imaginary component of J_n is increased while the other component is held constant. Notably, when the imaginary part of J_n becomes sufficiently large, e.g., $\ln[\text{Im}(J_n)] = 4$, variations in its real part no longer drive a transition between integrable and chaotic behavior. (b) With J_n fixed at $0.2i$, the system remains in the chaotic regime for small $|J_c|$. In contrast, a sufficiently large imaginary component of J_c suppresses the transition toward integrability, as indicated by the red line. For both panels, the parameters $(J_h, J_z, n) = (1, 0.5, 3)$, system size $N = 12$, and Hilbert-space dimension 6166 are kept fixed.

product state such as the Néel state,

$$|\text{Néel}\rangle = \bigotimes_{j=1}^{N/2} (|+1\rangle \otimes |-1\rangle), \quad (33)$$

shows rapid relaxation and the absence of revival, consistent with generic thermalization. Therefore, the tower states $\{|\psi_n(N, N-p)\rangle\}$ and their linear combinations constitute a scarred subspace that preserves coherent revivals even when the surrounding spectrum exhibits chaotic statistics.

IV. EXTENSION TO NON-HERMITIAN SYSTEMS

In this section, we focus on the non-Hermitian regime where the coupling strength is complex, and investigate quantum many-body scars within this framework. Similar to the Hermitian case, we first need to verify whether the system is non-integrable under non-Hermitian conditions. Here, since the Hamiltonian is non-Hermitian, its eigenvalue spectrum becomes complex. To characterize chaotic behavior in this regime, we employ the complex spacing ratio (CSR) analysis [34–36]. For a non-Hermitian Hamiltonian with complex eigenvalues $\{E_j\}$, we define

$$\lambda_j = \frac{E_j^{NN} - E_j}{E_j^{NNN} - E_j}, \quad (34)$$

where E_j^{NN} and E_j^{NNN} denote the nearest and next-to-nearest neighboring eigenvalues of E_j , respectively. By construction, $|\lambda_j| \leq 1$, and λ_j distributes inside the unit disk in the complex plane.

Following the analogy with the Berry–Tabor and Bohigas–Giannoni–Schmit conjectures, one expects that integrable systems exhibit CSR statistics identical to those of uncorrelated

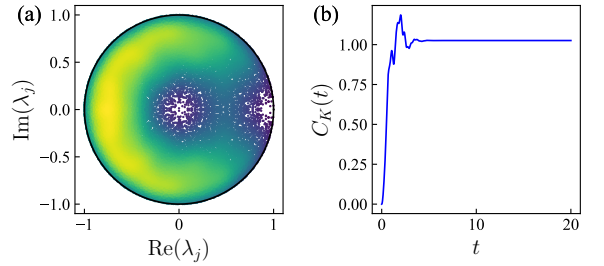


FIG. 7. Spectral distribution and Krylov complexity of the non-Hermitian Hamiltonian $\mathcal{H}_{M=0, k=0}$ with parameters $(J_h, J_c, J_n, n) = (1, 1, 0.2i, 3)$. Panel (a) shows the complex spacing ratio (CSR) statistics. The eigenvalues form a sparse distribution in the complex plane, yielding $\langle \cos \theta_j \rangle \approx -0.192$, characteristic of nonintegrable behavior. Panel (b) displays the corresponding Krylov complexity dynamics, which exhibits an initial rapid growth followed by decay and eventual saturation, a signature of chaotic evolution in non-Hermitian systems. Together, these results demonstrate that the introduction of a complex-valued long-range coupling H_n drives the system from integrability to chaos, consistent with the comparison to the $J_n = 0$ case in Fig. 3. Panel (a) corresponds to system size $N = 14$ with Hilbert-space dimension 44046, while panel (b) uses $N = 10$ with Hilbert-space dimension 902.

complex levels, while chaotic systems follow the Ginibre ensemble. In the integrable limit, the eigenvalues are independent, and the reference level does not influence its two nearest neighbors. Consequently, all ratios λ_j have equal probability, resulting in a uniform (flat) distribution over the unit circle. In contrast, for chaotic spectra obeying Ginibre statistics, level repulsion emerges: the ratio density vanishes at the origin and is suppressed at small angles, indicating the mutual repulsion of neighboring levels. A quantitative indicator is pro-

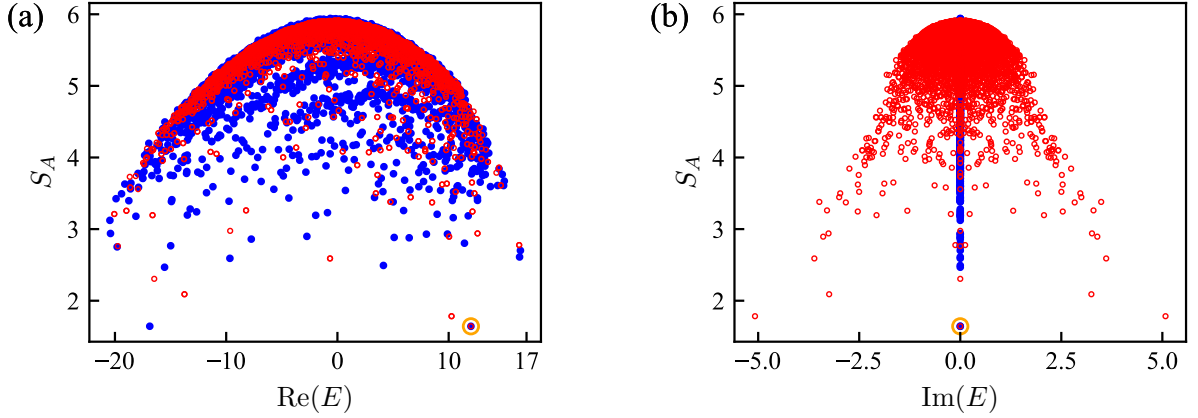


FIG. 8. Von Neumann entanglement entropy computed using Eq. (30) for the right eigenvectors of $\mathcal{H}_{M=0,k=0}$ with parameters $(J_h, J_c, J_z) = (1, 1, 0.5)$ and $n = 3$. The system size is $N = 12$, and the Hilbert-space dimension is 6166. Panels (a) and (b) show the dependence of the entanglement entropy on the real and imaginary parts of the eigenvalues, respectively. Blue dots correspond to the Hermitian case ($J_n = 0$), while red circles represent the non-Hermitian case ($J_n = 0.2i$). A common low-entanglement state appears in both parameter regimes (highlighted in orange), demonstrating the robustness of the quantum many-body scar against non-Hermitian perturbations.

vided by the angular average $\langle \cos \theta_j \rangle$, where $\theta_j = \arg(\lambda_j)$, which approaches $\langle \cos \theta_j \rangle \approx 0$ for integrable systems and $\langle \cos \theta_j \rangle \approx -0.24$ for chaotic systems in the thermodynamic limit [34]. For finite-size systems, these values are approximated but serve as clear diagnostics of the integrability-to-chaos transition.

In our previous study of the Hermitian case, we found that adjusting J_c and J_n can regulate the integrability of the system. Therefore, in this non-Hermitian case, we primarily focus on studying scenarios where J_c and J_n are complex numbers. First, we calculate the CSR and the related $\langle \cos \theta_j \rangle$ using Eq. (34) to determine how the integrable and chaotic characteristics vary with J_c and J_n . In Fig. 6, we plot two phase diagrams that show the relationship between $\langle \cos \theta_j \rangle$ and the other parameter when fixing J_c and J_n individually.

Building on this framework, we investigate two distinct scenarios: (i) the non-Hermitian transformation where introducing the complex term H_n converts a Hermitian integrable system into a non-Hermitian chaotic system, and (ii) the regime where both H_c and H_n possess complex-valued parameters, revealing that H_n induces an integrable-to-chaotic transition within non-Hermitian systems. We systematically analyze the quantum scarring characteristics in both cases, with particular emphasis on their dynamical manifestations.

A. Case I: Complex J_n

We now extend our analysis to non-Hermitian regimes by allowing the coupling J_n to take complex values, while keeping J_h , J_c , and J_z real. This introduces non-Hermiticity into the system and allows us to investigate whether the transition from integrability to chaos, previously observed in the Hermitian limit, persists in the complex parameter space.

We first analyze the non-Hermitian model with $(J_h, J_c, J_z, n) = (1, 1, 0.5, 3)$ and $J_n = 0.2i$. The results,

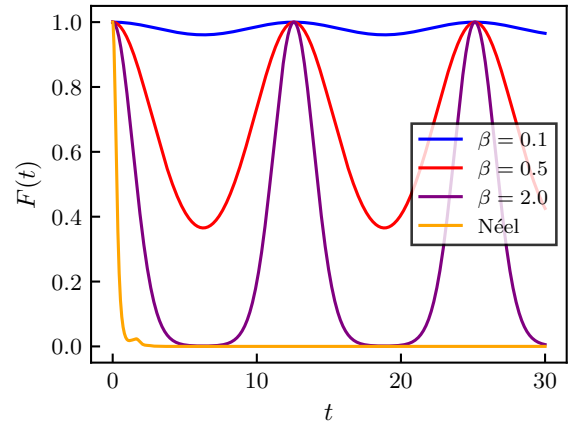


FIG. 9. Fidelity dynamics of the Hamiltonian H with parameters $(J_h, J_c, J_z, J_n, n) = (1, 1, 0.5, 0.2i, 3)$ under periodic boundary conditions, for a system size of $N = 8$ and Hilbert-space dimension is 6561. When the initial state is chosen as the coherent state defined in Eq. (31), clear periodic revivals are observed, indicating that this coherent state, or equivalently the tower of states defined in Eq. (16), exhibits the characteristic behavior of a quantum many-body scar. In contrast, for the Néel state, the fidelity decays rapidly to zero, signaling fast thermalization and the absence of scar dynamics.

summarized in Fig. 7, demonstrate that the introduction of an imaginary J_n drives the system from integrability to chaos. The left panel shows the time evolution of the Krylov complexity computed via Eq. (28), starting from an initial state given by an equal superposition of all eigenstates in the $(M, k) = (0, 0)$ subspace. The complexity first rises, then decays, and finally saturates, consistent with the dynamical signature of chaos. The right panel presents the CSR distribution in the complex plane, which displays the expected Ginibre-type repulsion pattern.

Having established the onset of chaos, we next explore whether the quantum many-body scar (QMBS) states identified in the Hermitian limit persist in this non-Hermitian setting. To this end, we compute the von Neumann entanglement entropy using Eq. (30) for the right eigenvectors of the non-Hermitian Hamiltonian. As shown in Fig. 8, even across the integrable-to-chaotic transition, a low-entropy state remains present. The coincidence between the low-entropy states in both the Hermitian ($J_n = 0$) and non-Hermitian ($J_n = 0.2i$) cases confirms the robustness of the scar tower described by Eq. (16).

Finally, to probe the dynamical properties of the scar states, we evaluate the fidelity dynamics of the coherent state defined in Eq. (31) and compare it with the Néel state. As shown in Fig. 9, the coherent state exhibits clear periodic revivals, while the Néel state rapidly thermalizes. These results confirm that the tower states $\{|\psi_n(N, N-p)\rangle\}$ continue to form a scar subspace even in the non-Hermitian chaotic regime.

In summary, *Case I* demonstrates that introducing a complex-valued nonlocal coupling J_n can drive the system from a Hermitian integrable phase to a non-Hermitian chaotic regime, as verified by both the CRS and Krylov-complexity diagnostics. To further reveal the universality of this mechanism, in the next subsection we extend our analysis to *Case II*, where the background Hamiltonian itself is already non-Hermitian (with complex J_c), and examine whether the same J_n -induced perturbation can again trigger the loss of integrability.

B. Case II: complex-valued J_c and J_n

In this subsection, we extend the analysis by allowing both J_c and J_n to take complex values. This generalization introduces an additional source of non-Hermiticity, thereby enriching the dynamical behavior of the model. As before, in order to identify potential quantum many-body scar states, we first need to confirm that the system exhibits non-integrable dynamics under certain parameter regimes.

To this end, we employ two complementary diagnostics: the level-spacing ratio defined in Eq. (34) and the Krylov complexity defined in Eq. (28). The results are summarized in Fig. 10. Specifically, panels (a) and (b) correspond to the case where $J_n = 0$, while panels (c) and (d) show results for $J_n = 0.2i$. The parameters are fixed as $(J_h, J_c, n) = (1, i, 3)$, and all calculations are performed within the $(M, k) = (0, 0)$ subspace of the Hamiltonian $\mathcal{H}_{M=0, k=0}$.

As J_n increases from zero to a finite imaginary value, the system undergoes a clear transition from integrability to chaos, similar to the Hermitian case. Having established the chaotic nature of the model in this parameter regime, we next explore the existence of quantum many-body scars.

To further characterize the structure of the eigenstates, we compute the von Neumann entanglement entropy according to Eq. (30), focusing on the right eigenvectors of $\mathcal{H}_{M=0, k=0}$. The results, displayed in Fig. 11, correspond to parameters $(J_h, J_c, J_z, n) = (1, i, 0.5, 3)$ for a system size of $N = 12$, within a Hilbert space of dimension 6166.

The presence of low-entanglement eigenstates that remain

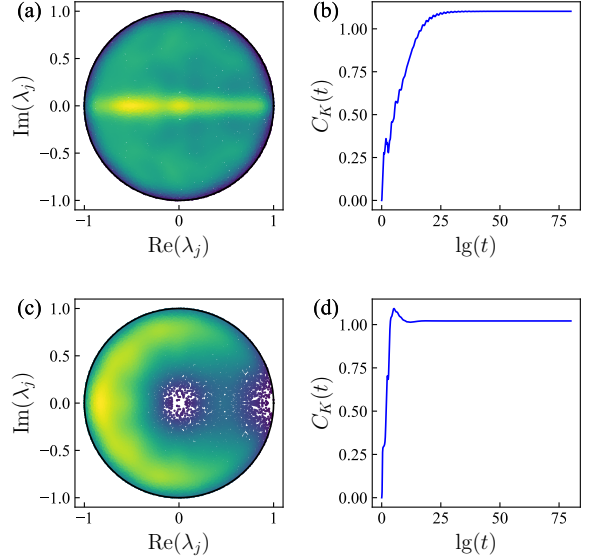


FIG. 10. Spectral and dynamical diagnostics of the non-Hermitian Hamiltonian $\mathcal{H}_{M=0, k=0}$ with parameters $(J_h, J_c, n) = (1, i, 3)$. Panels (a) and (b) display the CSR distribution and the time evolution of the Krylov complexity for $J_n = 0$, respectively. The CSR shows an approximately uniform distribution in the complex plane, with $\langle \cos \theta_j \rangle \approx -0.028$, and the Krylov complexity grows linearly before saturating, both consistent with integrable behavior. Panels (c) and (d) present the corresponding results for $J_n = 0.2i$. In this case, the spectral distribution becomes strongly nonuniform, with $\langle \cos \theta_j \rangle \approx -0.187$, and the Krylov complexity exhibits rapid growth followed by decay and eventual saturation, indicating the onset of chaotic dynamics. Panels (a) and (c) use a system size of $N = 14$ (Hilbert-space dimension 44046), while panels (b) and (d) use $N = 10$ (Hilbert-space dimension 902).

robust as J_n changes suggests the survival of a tower of scar states, consistent with the analytical structure described by Eq. (16). To probe their dynamical signatures, we evaluate the fidelity dynamics for both the coherent scar state $|\psi_\beta\rangle$ defined in Eq. (31) and the Néel state, as shown in Fig. 12.

These results collectively show that the tower states $\{|\psi_n(N, N-p)\rangle\}$ retain their scar-like behavior even in the presence of non-Hermiticity. The persistence of coherent revivals in fidelity and the appearance of low-entanglement states confirm that the underlying scar subspace remains robust against complex deformations of the coupling parameters.

The two cases considered above together establish a coherent picture of the non-Hermitian extension of our model. In *Case I*, the system evolves from a Hermitian integrable regime to a non-Hermitian chaotic one as the complex hopping J_n is introduced. In *Case II*, the starting point is already non-Hermitian but integrable (with complex J_c), and the same complex J_n again induces the transition to chaos. Despite the distinct backgrounds, both cases reveal that J_n acts as a universal source of nonintegrability, controlling the crossover from regular to chaotic dynamics. Remarkably, in both transitions the tower states survive as robust quantum many-body scars, indicating that the scar subspace is protected not only against Hermitian perturbations but also under generic non-Hermitian

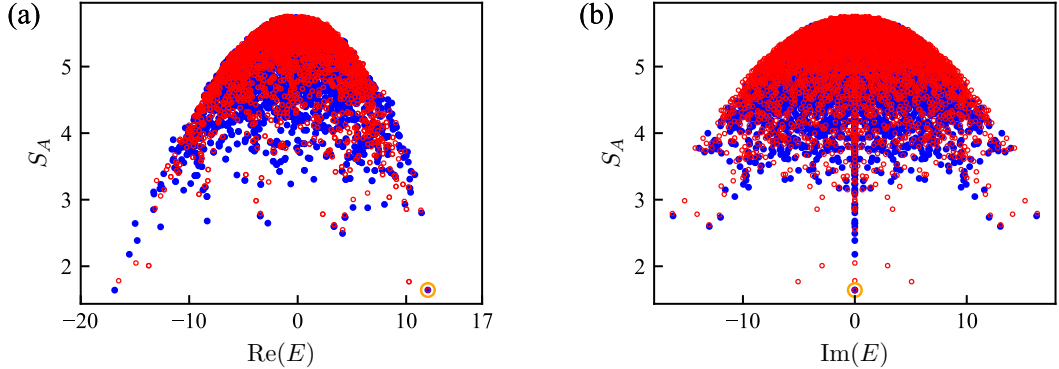


FIG. 11. Von Neumann entanglement entropy computed via Eq. (30) for the right eigenvectors of $\mathcal{H}_{M=0, k=0}$ with parameters $(J_h, J_c, J_z) = (1, i, 0.5)$ and $n = 3$. The system size is $N = 12$, with a Hilbert-space dimension of 6166. Panels (a) and (b) show the entanglement entropy plotted against the real and imaginary parts of the eigenvalues, respectively. Blue dots correspond to the Hermitian case ($J_n = 0$), while red circles represent the non-Hermitian case ($J_n = 0.2i$). In both parameter regimes, a common low-entanglement eigenstate appears (highlighted in orange), demonstrating the persistence and robustness of the quantum many-body scar under non-Hermitian perturbations.

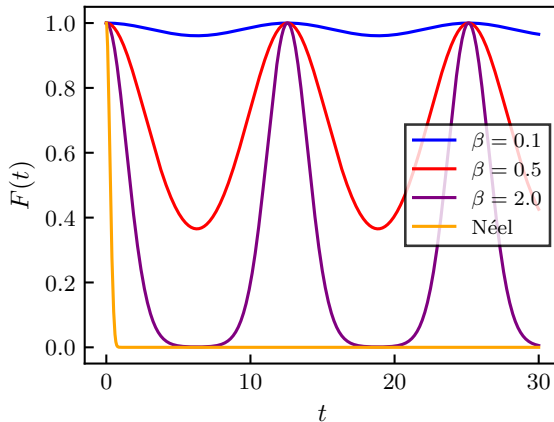


FIG. 12. Fidelity dynamics of the Hamiltonian H with parameters $(J_h, J_c, J_z, J_n, n) = (1, i, 0.5, 0.2i, 3)$ under periodic boundary conditions, for a system size of $N = 8$ and Hilbert-space dimension is 6561. When the initial state is chosen as the coherent state defined in Eq. (31), clear periodic revivals are observed, indicating that this coherent state, or equivalently the tower of states defined in Eq. (16), exhibits the characteristic behavior of a quantum many-body scar. In contrast, for the Néel state, the fidelity decays rapidly to zero, signaling fast thermalization and the absence of scar dynamics.

deformations.

V. SUMMARY AND OUTLOOK

In this work, we have systematically explored how the introduction of a long-range nonlocal hopping term H_n reshapes the integrability and dynamical behavior of both Hermitian and non-Hermitian spin chains. In the Hermitian regime, increasing J_n first drives the system from an integrable phase characterized by Poissonian level statistics to a chaotic phase

described by the Gaussian orthogonal ensemble, and eventually restores integrability at large J_n . Extending the model into the non-Hermitian domain reveals a unified mechanism: in *Case I*, a complex J_n transforms a Hermitian integrable system into a non-Hermitian chaotic one, whereas in *Case II*, an initially non-Hermitian but integrable system loses integrability once the complex long-range coupling is introduced. In both cases, J_n acts as a universal control parameter governing the transition from integrability to chaos.

Remarkably, despite these integrability-breaking transitions, a family of QMBS states persists throughout both Hermitian and non-Hermitian regimes, maintaining coherent oscillatory dynamics and revealing an unexpected robustness of nonthermal subspaces. This coexistence of chaos and scars highlights the intricate interplay between nonlocality, non-Hermiticity, and emergent order. Our results deepen the understanding of integrability breaking in complex quantum systems and pave a new way to controlling the quantum state in many-body systems.

DATA AVAILABILITY

The data that support the findings of this article are openly available [64].

ACKNOWLEDGMENTS

We are grateful for the numerical calculation library Quspin [65, 66] which has facilitated our research. We also acknowledge the support of the National Natural Science Foundation of China under Grants No. 12275193 and 11975166.

Appendix A: Proof that the Tower States are Eigenstates

In this appendix, we prove that the tower of ferromagnetic states, defined in the main text as Eq. (16) are exact eigenstates of the full Hamiltonian H . As shown in the main text, these states are trivially eigenstates of the SU(2)-symmetric Heisenberg term H_h , the chiral interaction H_c , and the Zeeman field H_z . The remaining task is to demonstrate that they are also eigenstates of the nonlocal hopping term H_n . For a fixed hopping distance n ($n \neq 0, N$ under PBCs), we define an operator (note that H_n is a Hermitian operator, while A_n is not).

$$A_n \equiv -iH_n = \sum_{j=1}^N (S_j^+ S_{j+n}^- - S_j^- S_{j+n}^+) . \quad (\text{A1})$$

If $|\psi(N, N-p)\rangle$ is an eigenstate of A_n , it is automatically an eigenstate of H_n . We now prove by induction that

$$A_n |\psi(N, N-p)\rangle = 0, \quad \forall p \geq 0. \quad (\text{A2})$$

For the fully polarized state $|\psi(N, N)\rangle = |\uparrow\rangle$,

$$A_n |\uparrow\rangle = \sum_{j=1}^N (S_j^+ S_{j+n}^- - S_j^- S_{j+n}^+) |\uparrow\rangle = 0, \quad (\text{A3})$$

since $S_j^+ |+1\rangle_j = 0$ and $S_{j+n}^+ |+1\rangle_{j+n} = 0$. Hence, $|\uparrow\rangle$ is annihilated by A_n .

The commutator between A_n and the total lowering operator $S^- = \sum_m S_m^-$ reads

$$[A_n, S^-] = \sum_{j=1}^N [(S_j^+ S_{j+n}^- - S_j^- S_{j+n}^+), S_j^- + S_{j+n}^-], \quad (\text{A4})$$

where operators on different sites commute. Using $[S_j^+, S_k^-] = 2\delta_{jk}S_j^z$ and $[S_j^-, S_k^-] = 0$, we obtain

$$[A_n, S^-] = 2 \sum_{j=1}^N (S_j^z S_{j+n}^- - S_j^- S_{j+n}^z). \quad (\text{A5})$$

Acting this on $|\uparrow\rangle$ gives

$$\begin{aligned} [A_n, S^-] |\uparrow\rangle &= 2 \sum_{j=1}^N (S_{j+n}^- - S_j^-) |\uparrow\rangle \\ &= 2 \left(\sum_{j=1}^N S_{j+n}^- - \sum_{j=1}^N S_j^- \right) |\uparrow\rangle. \end{aligned} \quad (\text{A6})$$

Under periodic boundary conditions, $\sum_j S_{j+n}^- = \sum_j S_j^-$, and therefore

$$[A_n, S^-] |\uparrow\rangle = 0. \quad (\text{A7})$$

Taking a further commutator yields

$$[[A_n, S^-], S^-] = 2 \sum_{j=1}^N [S_j^z S_{j+n}^- - S_j^- S_{j+n}^z, S_j^- + S_{j+n}^-]. \quad (\text{A8})$$

Each term in the summation cancels exactly, giving the operator identity

$$[[A_n, S^-], S^-] = 0. \quad (\text{A9})$$

Equations (A5) and (A9) imply that $[A_n, S^-] |\uparrow\rangle = 0$ and $[[A_n, S^-], S^-] = 0$. Let $X = [A_n, S^-]$; then $[X, S^-] = 0$, which means $[X, (S^-)^k] = 0$ for any $k \geq 1$. Applying this to $(S^-)^{p-1} |\uparrow\rangle$ yields

$$[A_n, S^-] (S^-)^{p-1} |\uparrow\rangle = 0. \quad (\text{A10})$$

Expanding the commutator gives

$$A_n (S^-)^p |\uparrow\rangle - S^- A_n (S^-)^{p-1} |\uparrow\rangle = 0. \quad (\text{A11})$$

It follows recursively that

$$A_n |\psi(N, N-p)\rangle = 0, \quad \forall p \geq 0. \quad (\text{A12})$$

Since $H_n = iA_n$, one has

$$H_n |\psi(N, N-p)\rangle = iA_n |\psi(N, N-p)\rangle = 0. \quad (\text{A13})$$

Therefore, the tower states $|\psi(N, N-p)\rangle$ are eigenstates of H_n with eigenvalue zero. Combined with their trivial eigenstate property under H_h , H_c , and H_z , this completes the proof that all $|\psi(N, N-p)\rangle$ are exact eigenstates of the full Hamiltonian H .

Appendix B: Bi-Lanczos Algorithm for Non-Hermitian Systems

In order to analyze the Krylov complexity in non-Hermitian quantum systems, we employ the bi-Lanczos algorithm, which generalizes the conventional Lanczos recursion to handle non-Hermitian Hamiltonians. The method constructs two biorthogonal Krylov bases, $\{|p_n\rangle\}$ and $\{|q_n\rangle\}$, corresponding to the right and left subspaces of the Liouvillian or Hamiltonian operator.

1. Algorithmic Construction

We start from an arbitrary normalized initial state $|\psi_0\rangle$, and define the initial vectors of the right and left Krylov subspaces as

$$|p_0\rangle = |\psi_0\rangle, \quad |q_0\rangle = |\psi_0\rangle, \quad (\text{B1})$$

with the normalization condition $\langle q_0 | p_0 \rangle = 1$.

At each recursion step n , we apply both the Hamiltonian H and its Hermitian conjugate H^\dagger to the basis vectors:

$$|p_{n+1}\rangle = H|p_n\rangle, \quad |q_{n+1}\rangle = H^\dagger|q_n\rangle. \quad (\text{B2})$$

To enforce biorthogonality, we define the Lanczos coefficients as

$$a_n = \langle q_n | p_{n+1} \rangle, \quad (\text{B3})$$

and remove the components along the previous two Krylov vectors,

$$|p_{n+1}\rangle \leftarrow |p_{n+1}\rangle - a_n|p_n\rangle - c_n|p_{n-1}\rangle, \quad (\text{B4})$$

$$|q_{n+1}\rangle \leftarrow |q_{n+1}\rangle - a_n^*|q_n\rangle - b_n^*|q_{n-1}\rangle, \quad (\text{B5})$$

where b_n and c_n are the normalization coefficients ensuring that $\langle q_{n+1}|p_{n+1}\rangle = 1$. Specifically,

$$b_n = \||p_{n+1}\rangle\|, \quad c_n = \langle q_{n+1}|p_{n+1}\rangle/b_n. \quad (\text{B6})$$

The vectors are then normalized as

$$|p_{n+1}\rangle \leftarrow \frac{|p_{n+1}\rangle}{b_n}, \quad |q_{n+1}\rangle \leftarrow \frac{|q_{n+1}\rangle}{c_n^*}. \quad (\text{B7})$$

In practice, due to the non-unitary evolution in non-Hermitian systems, small numerical errors can accumulate, breaking the biorthogonality condition. To mitigate this, a re-orthogonalization procedure is performed after each iteration, ensuring

$$\langle q_i|p_j\rangle = \delta_{ij}. \quad (\text{B8})$$

2. Effective Tridiagonal Representation

The bi-Lanczos recursion leads to a tridiagonal effective representation of the Hamiltonian in the biorthogonal Krylov basis:

$$H|p_n\rangle = b_{n+1}|p_{n+1}\rangle + a_n|p_n\rangle + c_n|p_{n-1}\rangle, \quad (\text{B9})$$

and similarly for the adjoint relation

$$H^\dagger|q_n\rangle = c_{n+1}^*|q_{n+1}\rangle + a_n^*|q_n\rangle + b_{n+1}^*|q_{n-1}\rangle. \quad (\text{B10})$$

Thus, the projected Hamiltonian in the Krylov subspace takes the matrix form

$$H_{\text{eff}} = \begin{pmatrix} a_0 & c_1 & 0 & \cdots & 0 \\ b_1 & a_1 & c_2 & \cdots & 0 \\ 0 & b_2 & a_2 & \cdots & 0 \\ \vdots & \vdots & \vdots & \ddots & c_{d-1} \\ 0 & 0 & 0 & b_{d-1} & a_{d-1} \end{pmatrix}. \quad (\text{B11})$$

3. Connection to Krylov Complexity

Once the biorthogonal Krylov bases $\{|p_n\rangle, |q_n\rangle\}$ are constructed, the time-evolved state can be expressed as

$$|\psi(t)\rangle = e^{-iHt}|\psi_0\rangle = \sum_n \phi_n(t)|p_n\rangle, \quad (\text{B12})$$

where the coefficients $\phi_n(t)$ obey a set of coupled differential equations governed by H_{eff} . The Krylov complexity, which measures the spread of the state in the Krylov basis, is then given by

$$C_K(t) = \sum_n n |\phi_n(t)|^2. \quad (\text{B13})$$

For non-Hermitian systems, both left and right Krylov amplitudes contribute, and the norm is generalized to $\langle\psi(t)|\psi(t)\rangle = \sum_n |\phi_n(t)|^2$ in the biorthogonal sense.

[1] Y. Jiao, Y. Zhang, J. Bai, S. Jia, C. S. Adams, Z. Bai, H. Shen, and J. Zhao, Photoionization-Induced Floquet Driving of a Discrete Time Crystal in a Thermal Rydberg Ensemble, *Phys. Rev. Lett.* 135, 163603 (2025).

[2] B. Lapierre, P. Moosavi, and B. Oblak, Nonequilibrium Probes of Quantum Geometry in Gapless Systems, *arXiv:2511.09639*.

[3] G. T. Landi, D. Poletti, and G. Schaller, Nonequilibrium boundary-driven quantum systems: Models, methods, and properties, *Rev. Mod. Phys.* 94, 045006 (2022).

[4] S. Mendizabal, Non-equilibrium scalar fields at finite temperature and density, *Annals of Physics* 170290 (2025).

[5] M. G. Skou, T. G. Skov, N. B. Jørgensen, K. K. Nielsen, A. Camacho-Guardian, T. Pohl, G. M. Bruun, and J. J. Arlt, Non-equilibrium quantum dynamics and formation of the Bose polaron, *Nat. Phys.* 17, 731 (2021).

[6] J. Yin, Y. Chan, F. H. da Jornada, D. Y. Qiu, C. Yang, and S. G. Louie, Analyzing and predicting non-equilibrium many-body dynamics via dynamic mode decomposition, *Journal of Computational Physics* 477, 111909 (2023).

[7] D. A. Abanin, E. Altman, I. Bloch, and M. Serbyn, Colloquium: Many-body localization, thermalization, and entanglement, *Rev. Mod. Phys.* 91, (2019).

[8] P. Reimann, Eigenstate thermalization: Deutsch's approach and beyond, *New J. Phys.* 17, 055025 (2015).

[9] M. Alishahiha and M. J. Vasli, Eigenstate Thermalization Hypothesis: A Short Review, *arXiv:2501.07243*.

[10] L. D'Alessio, Y. Kafri, A. Polkovnikov, and M. Rigol, From quantum chaos and eigenstate thermalization to statistical mechanics and thermodynamics, *Advances in Physics* 65, 239 (2016).

[11] T. Mori, T. N. Ikeda, E. Kaminishi, and M. Ueda, Thermalization and prethermalization in isolated quantum systems: a theoretical overview, *J. Phys. B: At. Mol. Opt. Phys.* 51, 112001 (2018).

[12] B. Buča, Unified Theory of Local Quantum Many-Body Dynamics: Eigenoperator Thermalization Theorems, *Phys. Rev. X* 13, (2023).

[13] M. Schecter and T. Iadecola, Weak Ergodicity Breaking and Quantum Many-Body Scars in Spin-1 XY Magnets, *Phys. Rev. Lett.* 123, (2019).

[14] Q.-Q. Wang et al., Experimental verification of generalized eigenstate thermalization hypothesis in an integrable system, *Light Sci Appl* 11, (2022).

[15] G. Zhang and Z. Song, Quantum scars in spin-1/2 isotropic Heisenberg clusters, *New J. Phys.* 25, 053025 (2023).

[16] T. Mori, T. N. Ikeda, E. Kaminishi, and M. Ueda, Thermalization and prethermalization in isolated quantum systems: a theoretical overview, *J. Phys. B: At. Mol. Opt. Phys.* 51, 112001 (2018).

- [17] S. Nandy, A. Sen, A. Das, and A. Dhar, Eigenstate Gibbs ensemble in integrable quantum systems, *Phys. Rev. B* 94, 245131 (2016).
- [18] D.-Z. Wang, H. Zhu, J. Cui, J. Argüello-Luengo, M. Lewenstein, G.-F. Zhang, P. Sierant, and S.-J. Ran, Eigenstate thermalization and its breakdown in quantum spin chains with inhomogeneous interactions, *Phys. Rev. B* 109, 045139 (2024).
- [19] M. Rigol, V. Dunjko, V. Yurovsky, and M. Olshanii, Relaxation in a Completely Integrable Many-Body Quantum System: An Ab Initio Study of the Dynamics of the Highly Excited States of 1D Lattice Hard-Core Bosons, *Phys. Rev. Lett.* 98, 050405 (2007).
- [20] D. A. Abanin, E. Altman, I. Bloch, and M. Serbyn, Colloquium: Many-body localization, thermalization, and entanglement, *Rev. Mod. Phys.* 91, 021001 (2019).
- [21] J. Z. Imbrie, V. Ros, and A. Scardicchio, Local integrals of motion in many-body localized systems, *Annalen Der Physik* 529, 1600278 (2017).
- [22] S. Moudgalya, B. A. Bernevig, and N. Regnault, Quantum many-body scars and Hilbert space fragmentation: a review of exact results, *Rep. Prog. Phys.* 85, 086501 (2022).
- [23] K. Omiya, Quantum many-body scars as remnants of stable many-body periodic orbits, *Phys. Rev. B* 111, 245158 (2025).
- [24] A. Kerschbaumer, M. Ljubotina, M. Serbyn, and J.-Y. Desaules, Quantum Many-Body Scars beyond the PXP Model in Rydberg Simulators, *Phys. Rev. Lett.* 134, 160401 (2025).
- [25] B. Evrard, A. Pizzi, S. I. Mistakidis, and C. B. Dag, Quantum many-body scars from unstable periodic orbits, *Phys. Rev. B* 110, 144302 (2024).
- [26] A. Chandran, T. Iadecola, V. Khemani, and R. Moessner, Quantum Many-Body Scars: A Quasiparticle Perspective, *Annu. Rev. Condens. Matter Phys.* 14, 443 (2023).
- [27] C. J. Turner, A. A. Michailidis, D. A. Abanin, M. Serbyn, and Z. Papić, Weak ergodicity breaking from quantum many-body scars, *Nature Phys* 14, 745 (2018).
- [28] V. I. Yukalov, Equilibration and thermalization in finite quantum systems, *Laser Phys. Lett.* 8, 485 (2011).
- [29] H. Eleuch and I. Rotter, Nearby states in non-Hermitian quantum systems I: Two states, *Eur. Phys. J. D* 69, 229 (2015).
- [30] H. Eleuch and I. Rotter, Open quantum systems and Dicke superradiance, *Eur. Phys. J. D* 68, 74 (2014).
- [31] A. Frisk Kockum, A. Miranowicz, S. De Liberato, S. Savasta, and F. Nori, Ultrastrong coupling between light and matter, *Nat Rev Phys* 1, 19 (2019).
- [32] E. Medina-Guerra, I. V. Gornyi, and Y. Gefen, Correlations and Krylov spread for a non-Hermitian Hamiltonian: Ising chain with a complex-valued transverse magnetic field, *Phys. Rev. B* 111, 174207 (2025).
- [33] I. Rotter, Non-Hermitian Quantum Physics of Open Systems, *arXiv:1707.03298*.
- [34] L. Sá, P. Ribeiro, and T. Prosen, Complex Spacing Ratios: A Signature of Dissipative Quantum Chaos, *Phys. Rev. X* 10, 021019 (2020).
- [35] M. Baggioli, K.-B. Huh, H.-S. Jeong, X. Jiang, K.-Y. Kim, and J. F. Pedraza, Singular value decomposition and its blind spot for quantum chaos in non-Hermitian Sachdev-Ye-Kitaev models, *Phys. Rev. D* 111, L101904 (2025).
- [36] Q. Chen, S. A. Chen, and Z. Zhu, Weak ergodicity breaking in non-Hermitian many-body systems, *SciPost Physics* 15, 052 (2023).
- [37] K. Kawabata, Z. Xiao, T. Ohtsuki, and R. Shindou, Singular-Value Statistics of Non-Hermitian Random Matrices and Open Quantum Systems, *PRX Quantum* 4, 040312 (2023).
- [38] T. Iadecola and M. Schecter, Quantum many-body scar states with emergent kinetic constraints and finite-entanglement revivals, *Phys. Rev. B* 101, 024306 (2020).
- [39] B. Bertini, F. Heidrich-Meisner, C. Karrasch, T. Prosen, R. Steinigeweg, and M. Žnidarič, Finite-temperature transport in one-dimensional quantum lattice models, *Rev. Mod. Phys.* 93, 025003 (2021).
- [40] L. F. Santos, Integrability of a disordered Heisenberg spin-1/2 chain, *J. Phys. A: Math. Gen.* 37, 4723 (2004).
- [41] A. Gubin and L. F. Santos, Quantum chaos: An introduction via chains of interacting spins 1/2, *Am. J. Phys.* 80, 246 (2012).
- [42] R. Steinigeweg, J. Gemmer, and W. Brenig, Spin and energy currents in integrable and nonintegrable spin- $\frac{1}{2}$ chains: A typicality approach to real-time autocorrelations, *Phys. Rev. B* 91, 104404 (2015).
- [43] F. Heidrich-Meisner, A. Honecker, and W. Brenig, Transport in quasi one-dimensional spin-1/2 systems, *Eur. Phys. J. Spec. Top.* 151, 135 (2007).
- [44] M. Žnidarič, Weak Integrability Breaking: Chaos with Integrability Signature in Coherent Diffusion, *Phys. Rev. Lett.* 125, (2020).
- [45] X. He, B. Zhu, X. Li, F. Wang, Z.-F. Xu, and D. Wang, Coherent spin-mixing dynamics in thermal Rb 87 spin-1 and spin-2 gases, *Phys. Rev. A* 91, 033635 (2015).
- [46] M.-S. Chang, Q. Qin, W. Zhang, L. You, and M. S. Chapman, Coherent spinor dynamics in a spin-1 Bose condensate, *Nature Phys* 1, 111 (2005).
- [47] P. N. Jepsen, W. W. Ho, J. Amato-Grill, I. Dimitrova, E. Demler, and W. Ketterle, Transverse Spin Dynamics in the Anisotropic Heisenberg Model Realized with Ultracold Atoms, *Phys. Rev. X* 11, 041054 (2021).
- [48] Y.-A. Chen, S. Nascimbène, M. Aidelsburger, M. Atala, S. Trotzky, and I. Bloch, Controlling Correlated Tunneling and Superexchange Interactions with ac-Driven Optical Lattices, *Phys. Rev. Lett.* 107, 210405 (2011).
- [49] I. Dimitrova, N. Jepsen, A. Buyskikh, A. Venegas-Gomez, J. Amato-Grill, A. Daley, and W. Ketterle, Enhanced Superexchange in a Tilted Mott Insulator, *Phys. Rev. Lett.* 124, 043204 (2020).
- [50] S. Trotzky, P. Cheinet, S. Fölling, M. Feld, U. Schnorrberger, A. M. Rey, A. Polkovnikov, E. A. Demler, M. D. Lukin, and I. Bloch, Time-Resolved Observation and Control of Superexchange Interactions with Ultracold Atoms in Optical Lattices, *Science* 319, 295 (2008).
- [51] K. Sanada, Y. Miao, and H. Katsura, Quantum many-body scars in spin models with multibody interactions, *Phys. Rev. B* 108, 155102 (2023).
- [52] A. Micheli, G. K. Brennen, and P. Zoller, A toolbox for lattice-spin models with polar molecules, *Nature Phys* 2, 341 (2006).
- [53] H. P. Büchler, M. Hermele, S. D. Huber, M. P. A. Fisher, and P. Zoller, Atomic Quantum Simulator for Lattice Gauge Theories and Ring Exchange Models, *Phys. Rev. Lett.* 95, 040402 (2005).
- [54] I. Dimitrova, N. Jepsen, A. Buyskikh, A. Venegas-Gomez, J. Amato-Grill, A. Daley, and W. Ketterle, Enhanced Superexchange in a Tilted Mott Insulator, *Phys. Rev. Lett.* 124, 043204 (2020).
- [55] T. Ding et al., Nonlinear Coherence Effects in Transient-Absorption Ion Spectroscopy with Stochastic Extreme-Ultraviolet Free-Electron Laser Pulses, *Phys. Rev. Lett.* 123, 103001 (2019).
- [56] J. Yao, L. Lin, and M. Bukov, Reinforcement Learning for Many-Body Ground-State Preparation Inspired by Counterdiabatic Driving, *Phys. Rev. X* 11, 031070 (2021).

- [57] A. Schuckert, O. Katz, L. Feng, E. Crane, A. De, M. Hafezi, A. V. Gorshkov, and C. Monroe, Observation of a finite-energy phase transition in a one-dimensional quantum simulator, *Nat. Phys.* 21, 374 (2025).
- [58] Y. Y. Atas, E. Bogomolny, O. Giraud, and G. Roux, Distribution of the Ratio of Consecutive Level Spacings in Random Matrix Ensembles, *Phys. Rev. Lett.* 110, 084101 (2013).
- [59] Y. Zhou, W. Xia, L. Li, and W. Li, Diagnosing quantum many-body chaos in non-Hermitian quantum spin chain via Krylov complexity, *Phys. Rev. Res.* 7, 033281 (2025).
- [60] M. Baggio, K.-B. Huh, H.-S. Jeong, K.-Y. Kim, and J. F. Pedraza, Krylov complexity as an order parameter for quantum chaotic-integrable transitions, *Phys. Rev. Res.* 7, 023028 (2025).
- [61] C. Liu, H. Tang, and H. Zhai, Krylov complexity in open quantum systems, *Phys. Rev. Res.* 5, 033085 (2023).
- [62] K. Adhikari, S. Choudhury, and A. Roy, Krylov Complexity in Quantum Field Theory, *Nuclear Physics B* 993, 116263 (2023).
- [63] Q. Hu, W.-Y. Zhang, Y. Han, and W.-L. You, Krylov complexity in quantum many-body scars of spin-1 models, *Phys. Rev. B* 111, 165106 (2025).
- [64] Y. S. Liu and X. Z. Zhang, Zenodo <http://doi.org/10.5281/zenodo.17666493>
- [65] P. Weinberg and M. Bukov, QuSpin: a Python package for dynamics and exact diagonalisation of quantum many body systems part I: spin chains, *SciPost Physics* 2, 003 (2017).
- [66] P. Weinberg and M. Bukov, QuSpin: a Python package for dynamics and exact diagonalisation of quantum many body systems. Part II: bosons, fermions and higher spins, *SciPost Physics* 7, 020 (2019).